Atmos. Meas. Tech. Discuss., 8, 4379–4412, 2015
www.atmos-meas-tech-discuss.net/8/4379/2015/
doi:10.5194/amtd-8-4379-2015

Atmospheric Measurement Techniques Discussions
Open Access

Infrared limb emission measurements of aerosol in the troposphere and stratosphere

S. Griessbach[1], L. Hoffmann[1], R. Spang[2], M. von Hobe[2], R. Müller[2], and M. Riese[2]

[1]Jülich Supercomputing Centre (JSC), Forschungszentrum Jülich GmbH, 52425 Jülich, Germany
[2]Institute of Energy and Climate Research (IEK-7), Forschungszentrum Jülich GmbH, 52425 Jülich, Germany

Received: 27 February 2015 – Accepted: 23 March 2015 – Published: 29 April 2015

Correspondence to: S. Griessbach (s.griessbach@fz-juelich.de)

Published by Copernicus Publications on behalf of the European Geosciences Union.

Abstract

Altitude resolved aerosol detection in the upper troposphere and lower stratosphere (UTLS) is a challenging task for remote sensing instruments. Here, we introduce a new method for detecting aerosol in the UTLS based on infrared limb emission measurements. The method applies an improved aerosol-cloud-index that indicates infrared limb spectra affected by aerosol and ice clouds. For the discrimination between aerosol and ice clouds we developed a new method based on brightness temperature difference correlations. The discrimination thresholds for the new method were derived from radiative transfer simulations (including scattering) and Michelson Interferometer for Passive Atmospheric Sounding (MIPAS)/Envisat measurements obtained in 2011. The method not only reliably separates aerosol from ice clouds, but also provides characteristic yet overlapping correlation patterns for volcanic ash and sulfate aerosol. We demonstrate the value of the new approach for volcanic ash and sulfate aerosol originating from the Grímsvötn (Iceland), Puyehue-Cordón Caulle (Chile) and Nabro (Eritrea) eruptions by comparing with Atmospheric Infrared Sounder (AIRS) volcanic ash and SO_2 measurements.

1 Introduction

Aerosol is omnipresent and highly variable in the atmosphere. The tropospheric aerosol can have a large impact on every day life. It occurs, for example, in the form of anthropogenic pollution aerosol e.g. reducing the visibility (Zhang et al., 2015), mineral dust fertilising the Amazon forest (Koren et al., 2006), or volcanic ash posing a danger to aircraft (Casadevall, 1994). Aerosol particles also serve as ice nuclei and hence influence cloud formation and precipitation (Fridlind et al., 2004; Yu et al., 2010; Yuan et al., 2011). Stratospheric aerosol, which is mainly sulfate aerosol, is significantly influenced by volcanic eruptions (Vernier et al., 2011). It has an impact on the radiation budget of the Earth and hence can influence climate (Santer et al., 2014; Ridley et al., 2014).

AMTD
8, 4379–4412, 2015

Aerosol measurements in the upper troposphere and stratosphere are available from a variety of sources. In particular, satellite measurements provide global climatologies and time series of stratospheric aerosol (Bauman et al., 2003; Vernier et al., 2011). However, most satellite instruments measuring in the ultraviolet and visible (UV/VIS) range have limitations regarding measurements at nighttime (including polar night) and, due to the challenging discrimination between aerosol and ice clouds, many aerosol products are only available above 15 km (Ridley et al., 2014). In contrast, infrared (IR) instruments provide a global coverage at day- and nighttime during all seasons and several methods are available for nadir instruments to discriminate between ice clouds and various aerosol types (Karagulian et al., 2010; Clarisse et al., 2010, 2013).

Limb measurements in the IR are highly sensitive towards aerosol and additionally provide information on the vertical distribution. It has been shown that the stratospheric sulfate aerosol after the Mt. Pinatubo eruption introduces a characteristic spectral signature into IR limb spectra for the Improved Stratospheric And Mesospheric Sounder (ISAMS) (Grainger et al., 1993; Lambert et al., 1993), the Cryogenic Limb Array Etalon Spectrometer (CLAES) (Massie et al., 1996; Lambert et al., 1997), and the balloon-borne Michelson Interferometer for Passive Atmospheric Sounding (MIPAS-B) (Echle et al., 1998). Further, Echle et al. (1998) derived optical and microphysical parameters of stratospheric aerosol from MIPAS-B measurements. However, since these studies are restricted to the stratosphere they do not consider ice clouds or other aerosol types. Studies using high resolution IR spectra of the space-borne IR limb instruments Cryogenic Infrared Spectrometers and Telescopes for the Atmosphere (CRISTA) (Offermann et al., 1999; Riese et al., 1999) and Michelson Interferometer for Passive Atmospheric Sounding (MIPAS) (Fischer et al., 2008) present methods to distinguish between the three types of polar stratospheric clouds (PSCs) (ice, supercooled ternary solutions, and nitric acid trihydrate) (Spang and Remedios, 2003; Spang et al., 2004, 2005, 2012; Höpfner et al., 2009). Yet, these methods are restricted to the stratosphere.

For the detection and classification of aerosol in the troposphere with IR limb measurements methods are rare. For the detection of clouds and aerosol in the troposphere

AMTD
8, 4379–4412, 2015

and stratosphere Spang et al. (2001) introduced the cloud index (CI) for CRISTA. Later, the CI was adapted to MIPAS (Spang et al., 2004) and to the air-borne CRISTA-New Frontiers (CRISTA-NF) (Spang et al., 2008) and the MIPAS CI thresholds were optimised depending on latitude and altitude (Sembhi et al., 2012). A first attempt to classify between tropospheric ice and liquid clouds in MIPAS spectra is made by Spang et al. (2012). Regarding the discrimination between ice clouds and aerosol and the classification of aerosol, Griessbach et al. (2012, 2014) presented a method to detect volcanic ash in the troposphere and stratosphere with MIPAS. Also for MIPAS Grainger et al. (2013) presented methods to identify volcanic plumes containing sulfur dioxide, sulfate aerosol and volcanic ash.

Hitherto, for IR limb measurements there are no general aerosol detection algorithms. However, IR nadir classification techniques demonstrate the capability of IR measurements to provide a discrimination between ice clouds and aerosol. Discriminating between aerosol and ice clouds in limb measurements would also offer the opportunity to study the aerosol in the upper troposphere as well as the stratosphere. In the past, the impact of volcanic aerosol on radiative forcing in the lower stratosphere at high and mid latitudes has been underestimated, chiefly due to the lack of measurements in this region (Ridley et al., 2014).

Here, we present a method to detect aerosol in the troposphere and stratosphere and to discriminate it from ice clouds with infrared limb emission measurements. The paper describes the method and shows examples for altitude resolved aerosol detection. First, we present the instruments and our radiative transfer model (Sect. 2). Then we introduce a method that allows the detection of aerosol and clouds in the troposphere as well as in the stratosphere (Sect. 3.1). Starting with the new aerosol and cloud detections we develop a method to distinguish between ice clouds and aerosol (Sect. 3.2). We apply the new method to MIPAS measurements in 2011 and present the results for three volcanic eruptions, the Grímsvötn (Iceland), Puyehue-Cordón Caulle (Chile) and the Nabro (Eritrea) eruption, and compare them with Atmospheric Infrared

AMTD
8, 4379–4412, 2015

Sounder (AIRS) SO_2 and volcanic ash measurements (Sect. 4). Finally, we present our conclusions (Sect. 5).

2 Instruments and forward model

2.1 MIPAS

The infrared limb sounder MIPAS measures high-resolution spectra in the thermal infrared between 685 and 2410 cm^{-1} (Fischer et al., 2008). In our study we use the measurements of band A (685–970 cm^{-1}) and band B (1215–1500 cm^{-1}). MIPAS is mounted on ESA's Envisat and measured atmospheric profiles between 6 to 68 km altitude from July 2002 to March 2004 and 7 to 72 km altitude from January 2005 to April 2012 in its nominal mode. Since MIPAS measures in the thermal infrared from a nearly polar orbit it covered the whole Earth at day- and nighttime. Due to a malfunction in 2004 MIPAS' original nominal operation mode, which comprised a spectral sampling of 0.025 cm^{-1} and a vertical sampling of 3 km, had to be changed. In 2005 the spectral sampling was reduced to 0.0625 cm^{-1} and the vertical sampling below 20 km was increased to 1.5 km. Also the measurement geometry was modified so that MIPAS samples down to 7 km in the polar regions and down to 10 km in the tropics (Fischer et al., 2008). For developing a method to detect aerosol and to demonstrate its viability we use MIPAS level 1b calibrated radiances that are available at ESA (2015).

2.2 AIRS

For the comparison with the MIPAS aerosol measurements we use the AIRS level 1b radiances that are available at http://airs.jpl.nasa.gov/ . The infrared nadir sounder AIRS (Aumann et al., 2003) is mounted on NASA's Aqua satellite launched in May 2002. The AIRS hyperspectral infrared spectra between 3.7–15.4 µm (649–2674 cm^{-1}) are obtained from measurements in the nadir and sub-limb observation

AMTD
8, 4379–4412, 2015

geometry. Each scan consists of 90 footprints in the across-track direction and covers a distance of 1765 km on the ground. The footprint size is 13.5 km × 13.5 km for nadir and 41 km × 21.4 km for the outermost sub-limb views. AIRS measures 14.5 orbits comprising about 2.9 million spectra per day. This provides an excellent horizontal resolution with global coverage twice a day except for small gaps at mid and low latitudes.

2.3 JURASSIC

For radiative transfer simulations of the MIPAS measurements we use the Juelich Rapid Spectral Simulation Code (JURASSIC) (Hoffmann et al., 2008). It applies the emissivity growth approximation (Gordley and Russell, 1981) for fast simulations in the mid-infrared spectral region. JURASSIC has been used for radiative transfer simulations and trace gas retrievals for various infrared limb instruments (Hoffmann et al., 2008, 2009; Weigel et al., 2010; Ungermann et al., 2010) and for nadir sounder such as AIRS (Hoffmann and Alexander, 2009; Grimsdell et al., 2010).

JURASSIC has been extended with a scattering module that allows for radiative transfer simulations including single and multiple scattering on aerosol and cloud particles (Grießbach, 2012; Griessbach et al., 2013). In this study, we use Mie-calculations to calculate the optical properties extinction coefficient, scattering coefficient, and phase function. For the simulations presented here, we use a setup described in detail by Griessbach et al. (2014) with slight modifications. Here, the spectral sampling is 0.0625 cm^{-1} and the vertical sampling is 0.5 km. The setup of the cloud and aerosol layers and the atmosphere remains unchanged.

AMTD
8, 4379–4412, 2015

3 Aerosol detection and classification

3.1 Improved aerosol and cloud detection

The CI is the standard method to detect clouds and aerosol with MIPAS (Spang et al., 2001). It is defined as the ratio between the mean radiances around the 792 cm^{-1} band with strong CO_2 emissions and the atmospheric window region around 833 cm^{-1}:

$$CI = \frac{\bar{I}_1([788.25, 796.25\,cm^{-1}])}{\bar{I}_2([832.31, 834.37\,cm^{-1}])}, \quad (1)$$

with $\bar{I}_{1,2}$ the mean radiance of each window. CI values below 1.8–6 indicate cloudy air and CI values above 6 indicate clear air (Spang et al., 2004, 2012; Sembhi et al., 2012). The CI detection threshold depends on altitude and season, mainly because of variable water vapour content (Spang et al., 2004; Sembhi et al., 2012). Aiming at altitude and season independent aerosol detection we looked for additional windows in MIPAS band A. Figure 1 shows radiances between about 7 and 25 km altitude for a clear air profile. Bright colours indicate high radiances due to trace gas emissions and dark colours indicate atmospheric window regions with low radiances. These atmospheric windows are especially suited for aerosol detection, because trace gases have little impact here. The broad window around 830 cm^{-1} with low radiances at all altitudes is already used for the CI. Between about 940 and 970 cm^{-1} there are many narrow windows with small radiances between CO_2 lines. The broadest of these windows is located between 960 and 961 cm^{-1}. Therefore, we average over these 17 spectral points measured by MIPAS in this window and define the aerosol index (AI)

$$AI = \frac{\bar{I}_1([788.25, 796.25\,cm^{-1}])}{\bar{I}_2([960.00, 961.00\,cm^{-1}])} \quad (2)$$

with $\bar{I}_{1,2}$ the mean radiance of each window.

AMTD
8, 4379–4412, 2015

The AI is sensitive to aerosol and clouds, but in contrast to the CI it provides a better contrast to clear air due to less impact of the water vapour continuum around 960 cm^{-1}. A comparison between the CI and the AI is shown in Fig. 2a and b for one orbit measured on 18 August 2011, where most of the Northern Hemisphere was covered by a sulfate aerosol layer from the Nabro eruption in June 2011 (Bourassa et al., 2012; Fromm et al., 2014). The CI decreases with decreasing altitude, also for clear air conditions as in profiles 1–4 and 54–61. In regions with CI < 2 there are certainly ice clouds (Spang et al., 2004). For regions with 2 < CI < 6 it depends on the altitude, latitude and season if these CI values indicate aerosol or clouds. Hence, it is not apparent at first glance that the CI values between 4–5 on top of the tropospheric clouds in the Northern Hemisphere indicate the presence of Nabro aerosol. For the AI we see that in clear air regions the AI remains above 7. The tropospheric clouds have AI values below about 4 and on top of the tropospheric clouds there is a detached layer with AI values of 5–7. Below the stratospheric aerosol layer we can identify clear air regions, which was not possible using the CI. From visual inspection of all MIPAS orbits in 2011 we found that an AI of 7 is an appropriate threshold to distinguish between clear air and enhanced aerosol in the UTLS.

Although the AI provides a better contrast between clear air and aerosol and clouds in the UTLS, it has limitations at altitudes above about 25 km. In the middle stratosphere between about 30–45 km altitude the AI values can fall below 7. We observed a strong seasonal cycle for AI values below 7 in the middle stratosphere. In the summer hemisphere and at daytime (between 10 to 12 local time) the AI values fall below 7 whereas in the winter hemisphere and at nighttime (between 22 to 0 local time) the AI values are often above 7. This pattern extends down to about 25 km. This diurnal cycle and the differences between the summer and the winter hemisphere are most likely caused by non-local thermodynamic equilibrium (non-LTE) effects of the CO_2 laser bands between 950 and 970 cm^{-1} (Fig. 1). To provide a reliable aerosol and cloud detection in the troposphere and stratosphere we combine the advantages of the AI in the

AMTD
8, 4379–4412, 2015

troposphere and the CI in the stratosphere and define the aerosol cloud index (ACI):

$$\mathrm{ACI} = \max(\mathrm{CI}, \mathrm{AI}). \quad (3)$$

The ACI profiles (Fig. 2c) generally are the AI (Fig. 2b) at altitudes below 22 km and switch to the CI (Fig. 2a) at altitudes above 22 km.

To further confirm the ACI threshold value of 7 that we derived from the MIPAS measurements we investigated the behaviour of simulated ACI profiles for clear air conditions in four atmosphere types (Northern Hemisphere polar winter, polar summer, mid-latitude, equatorial atmosphere, Remedios et al., 2007). We found that in all atmospheres, except for the polar winter, the ACI values get smaller than 7 below 8.5 km in the equatorial atmosphere and below 5.5 km in the mid-latitude and polar summer atmosphere. This finding generally does not affect the measurements between 2005 and 2012, because of the modified measurement geometry that was designed to follow the tropopause and therefore reaches down to 6 km at the poles and 10 km in the tropics. In the measurements before 2005, where MIPAS measured down to 5 km, we did not observe ACI values below 7 at low altitudes regularly. We rather found a significant number of detections with ACI values larger than 10 in all climate zones. Sensitivity tests revealed that the simulations below approximately 10 km are highly affected by the water vapour continuum. In JURASSIC the Mlawer–Tobin–Clough–Kneizys–Davies 1.10 scheme (MT_CKD) (Clough et al., 2005), which is considered to represent real conditions with insufficient accuracy (Griessbach et al., 2013), is used for the water vapour continuum. This is most likely the explanation for the differences between the simulations and observations below 10 km. Hence, we conclude from the empirical analysis of the MIPAS measurements alone that an ACI value below 7 is an indicator for enhanced aerosol at altitudes above 5 km, but considering the simulation results we recommend to be careful with analyses at altitudes between 5–10 km, especially in the tropics.

AMTD
8, 4379–4412, 2015

3.2 Aerosol and ice classification

3.2.1 Window selection

For the discrimination between aerosol and ice clouds we choose appropriate windows, in which the optical properties of ice and aerosol differ most strongly. The optical properties, i.e. extinction coefficient (β_e) and single scattering albedo, are determined by the microphysical properties of the particles, i.e. complex refractive index, particle size, and particle shape. The real and imaginary parts of the complex refractive indices of ice (Warren and Brandt, 2008), sulfate aerosol (Hummel et al., 1988), and two types of volcanic ash (Volz, 1973, volcanic ash), (Pollack et al., 1973, basalt) are shown in Fig. 3a and b. As described in Sect. 3.1 we identified three window regions at:

- 830.6–831.1 cm^{-1}
- 960.0–961.0 cm^{-1}
- 1224.1–1224.7 cm^{-1}.

in which the contributions of atmospheric trace gases are at a minimum to avoid interferences of the aerosol signal with strong gas lines. These windows we refer to as the 830, 960, and 1224 cm^{-1} windows hereafter. In Fig. 3 they are indicated by grey bars. These windows are chosen to exploit the differences in the spectral gradients of aerosol (sulfate aerosol and volcanic ash) and ice clouds. For the first two windows, which are very close to the windows used for the volcanic ash detection reported by Griessbach et al. (2014), the spectral gradient of the imaginary part of the ice refractive indices is opposite to the one for sulfate aerosol and volcanic ash. The spectral gradient of the imaginary part from the first and second window to the third window is opposite for ice and sulfate aerosol. For the real part, the gradients of ice and volcanic ash are opposite for the first and second window and the spectral gradient from the first and second window to the third for ice is opposite for sulfate aerosol and ash.

AMTD
8, 4379–4412, 2015

These differences in the complex refractive index spectra between ice clouds and aerosol (volcanic ash and sulfate aerosol) propagate to the optical properties shown in Fig. 3c and d. To calculate the extinction coefficient and single scattering albedo we used the same log-normal size distributions as Griessbach et al. (2014) for sulfate aerosol, volcanic ash, sub-visible cirrus (small ice particles) and tropical cirrus (large ice particles). The extinction coefficient spectra were normalised to 1 at 960 cm^{-1}. For sulfate aerosol and ash they exhibit the same spectral gradients as the imaginary part of the refractive index. However, in addition to the refractive indices, the particles sizes have an impact on the optical properties. For large ice particles the extinction coefficient spectrum is flat and for small ice particles it exhibits a pronounced minimum around 960 cm^{-1}. The single scattering albedo shows that the scattering contribution to the extinction ranges from 30 to 80 % for small ice particles and is around 55 % for large ice particles. The scattering contribution of the sulfate aerosol is generally below 10 % and for volcanic ash it ranges from 15 to 80 %.

3.2.2 Measurements

Having identified three window regions with small radiance contributions by atmospheric trace gases and with significant differences in the optical properties for ice and aerosol, we expected that these differences could also be found in the radiance spectra measured by MIPAS. To relate the three windows to each other, we calculated brightness temperature differences (BTDs) from the radiances. The clearest correlation patterns were found for the BTDs between the 830 and 1224 cm^{-1} windows and the 960 and 1224 cm^{-1} windows. In Fig. 4 the BTDs are shown for four selected days (about 14 orbits) and regions where we expected to find four prototype scenarios: ice clouds only in Fig. 4a, Nabro sulfate aerosol in Fig. 4b, Puyehue Cordón-Caulle volcanic ash in Fig. 4c, and non-ice polar stratospheric clouds in Fig. 4d. The four scenarios differ. For ice clouds the spectra with an ACI below 7 form a relatively narrow group with BTDs between 0 and −40 K on both axes. For the sulfate aerosol, which has ACIs between 5 and 7 in Fig. 2, we now see a second cluster between −30 and −50 K on

AMTD
8, 4379–4412, 2015

the abscissa and −20 to −40 K on the ordinate. The volcanic ash forms an arc-shaped structure in the BTD diagram and for the non-ice PSCs there is a second cluster, which has smaller absolute BTDs than ice on the ordinate.

We analysed the 2011 MIPAS data on a day-by-day basis and used monthly and annual count statistics to estimate the threshold functions for a discrimination between ice clouds and aerosol. For ACI values below 4 the upper edge of the ice cluster is very sharp and we found the following threshold function:

$$BTD_{960-1224} = 0.87 \times BTD_{830-1224} + 6\,K. \quad (4)$$

For ACI values above 4 the BTD scatter plot can become quite diffuse for 2011, because there were three volcanic eruptions (Grímsvötn, Puyehue Cordón-Caulle, Nabro) that injected a substantial amount of aerosol into the atmosphere. We also analysed the measurements from 2003, a year with very few volcanic emissions during the MIPAS measurement period. For BTDs below −30.4 K we obtained the following threshold function:

$$BTD_{960-1224} = 1.33 \times BTD_{830-1224} + 20\,K. \quad (5)$$

To identify aerosol in the MIPAS data we used the condition that the BTDs must exceed at least one of the two threshold functions (in Fig. 4 the black solid lines must be exceeded). The result of this classification method is shown in Fig. 2d for a single MIPAS orbit. After colour coding all ACI values below 7 that indicate the presence of ice particles in grey, the Nabro sulfate aerosol layer clearly stands out (as well as a few non-ice PSCs in the South Pole region).

3.2.3 Simulations

To support the choice of the threshold functions and to further understand the characteristic patterns in the BTD correlation plots, we performed radiative transfer simulations for clear air, ice, volcanic ash and sulfate aerosol under various atmospheric

AMTD
8, 4379–4412, 2015

conditions. For the simulations we used JURASSIC with its internal Mie module and assumed spherical particles. We placed 1 km thick clouds at 7, 10, 14 and 18 km altitude and assumed various realistic combinations of particle sizes, concentrations and extinctions given at 948.5 cm^{-1} (see Tables 3–5 in Griessbach et al., 2014). We used the same setup as in Griessbach et al. (2014), where all details are given, but with an improved vertical sampling of 0.5 km (instead of 1 km). In Fig. 5 the simulation results are shown for all realistic ice cloud, aerosol and clear air scenarios for tangent altitudes ranging from 6 to 19.5 km, which covers the range from above to below the clouds. Except for the clear air simulations only the scenarios that have an ACI < 7 are shown.

The narrow ice pattern below the threshold functions that we found in the measurements is mostly reproduced by the ice cloud simulations in Fig. 5a. Especially for ACI values below 2 simulations and measurements agree well. However, for higher ACI values there are plenty of scenarios that fall in a range that was not covered by the measurements (about 0 to −40 K on the abscissa and −20 to −50 K on the ordinate). These scenarios have in common that their median radius is 6 µm or smaller and the extinction coefficient is smaller than or equal to 1×10^{-2} km^{-1}. We considered such small ice particles to be likely for ice PSCs (Deshler et al., 1994) and possibly subvisible cirrus clouds (SVCs) (Iwasaki et al., 2007; de Reus et al., 2009; Frey et al., 2011). However, in the tropics and at mid-latitudes we could not find MIPAS measurements that fall into this range. Hence, according to the MIPAS measurements 1 km thick ice clouds with particle sizes smaller than 6 µm seem very unlikely in the tropics and at mid-latitudes. Only in the polar regions, which are excluded in Fig. 4a–c, we found MIPAS measurements that show the same BTDs as the ice cloud simulations for median radii down to 3 µm.

There are a few simulated scenarios in the tropical atmosphere for the 18 km ice cloud that slightly exceed the upper threshold function. These particular scenarios have median radii of 6 µm or less and their extinction coefficients are between 5×10^{-2} and 1 km^{-1}. In the tropics median radii of 6 µm or less can only be found in SVCs. However, SVCs do not have such high particle concentrations and extinctions (Iwasaki et al.,

AMTD
8, 4379–4412, 2015

2007; de Reus et al., 2009; Frey et al., 2011). Hence, in the inset of Fig. 5a the simulation results are shown only for ice particle size distributions with median radii larger than 6 µm. The pattern of these ice cloud simulations is now in very good agreement with the measurements shown in Fig. 4 and also confirms that all, but 7 out of 3333, scenarios fall below the threshold functions. These 7 scenarios occur only for the ice cloud at 18 km altitude in the tropics and they all have a BTD larger than −25 K on the abscissa. We checked the MIPAS measurements between 20(30)° N and 20(30)° S and found that in 48(62) out of 58 945(78 563) cloudy profiles in 2011 the upper threshold was exceeded (both 0.08 %). In 2003, a year with less volcanic aerosol, only 15(18) out of 56 375(74 767) (0.02–0.03 %) cloudy profiles exceeded the upper threshold. Although, we do not consider 0.02–0.08 % to be a strong evidence in the measurements that tropical high altitude clouds consisting of small ice particles could exceed the aerosol classification threshold, we would like to point out that there is at least the theoretical possibility.

The sulfate aerosol simulations shown in Fig. 5b form a group just above the lower threshold function. This group matches very well the sulfate aerosol observations after the Nabro eruption in Fig. 4b. There are also a few scenarios for which the simulated BTD does not exceed the aerosol detection threshold. These scenarios occur all at tangent altitudes below 8 km. Thus, we conclude that with the method introduced sulfate aerosol can be discriminated from ice clouds above 8 km. In contrast to the simulations we found numerous aerosol detections below 8 km altitude in the MIPAS measurements. This is most likely due to the fact that the aerosol layers in reality have a larger vertical extent than the 1 km assumed in the simulations. This effect is discussed in detail in a separate study (Griessbach et al., 2015). The simulations also showed that 1 km thick sulfate aerosol layers with an extinction coefficient of $1 \times 10^{-4}\,\mathrm{km}^{-1}$ at 947 cm^{-1} (10.5 µm) have ACIs larger than 7 and hence are not detectable with this method. For extinction coefficients of $5 \times 10^{-4}\,\mathrm{km}^{-1}$ and higher the ACI fell below 7 and the sulfate aerosol is detectable.

AMTD
8, 4379–4412, 2015

The simulations shown in Fig. 5c using basalt refractive indices (Pollack et al., 1973) represent the volcanic ash measurements shown in Fig. 4c after the Puyehue-Cordón Caulle eruption better than simulations using the volcanic ash refractive indices reported by Volz (1973). Thus, the volcanic ash simulations are very sensitive to the refractive index data. Figure 4c shows that with the introduced method not all volcanic ash, but a substantial fraction can be discriminated from ice clouds. The smaller the particle size, the more scenarios exceed the aerosol detection threshold. Griessbach et al. (2014) reported a maximum median radius of 1.5 µm for MIPAS volcanic ash (Volz, 1973) detections. Here, for volcanic ash and basalt we found some scenarios with a median radius of 5 µm that exceed the aerosol detection threshold. Although the aerosol detection method introduced is more sensitive to larger volcanic ash median radii, further criteria are required for the discrimination between e.g. sulfate aerosol and volcanic ash in order to unambiguously identify volcanic ash. From the simulations presented here, we derived that basalt and volcanic ash particles with median radii between 0.3 and 5 µm and extinction coefficients between 1×10^{-3} and 5×10^{-1} km^{-1} can be discriminated from ice clouds at altitudes down to 6 km.

The clear air simulations in Fig. 5d for the four atmospheres (polar winter, polar summer, mid-latitudes, equatorial) at altitudes between 6 to 19.5 km illustrate that the ACI criterion is required as a pre-filter for the detection of aerosol. While all of the clear air scenarios at altitudes below 14 km altitude already fall below the threshold functions, some scenarios above 14 km lie above the thresholds. These can easily be filtered by using the ACI criterion. The clear air simulations also show that for the polar summer, mid-latitude and equatorial atmospheres the ACI falls below 7 at altitudes below 7.5, 7.5 and 9.5 km, respectively. However, this simulated behaviour is not completely in agreement with the MIPAS measurements in 2003, where measurements were made down to 6 km at all latitudes and no systematic decrease of the ACI value with decreasing altitude was observed. Sensitivity tests showed that the ACI simulations below 7.5 km at high and mid-latitudes and 9.5 km in the tropics are affected by the water vapour continuum. Further studies would be required to determine if the decrease of the ACI is

AMTD
8, 4379–4412, 2015

a simulation artefact, either due to the assumed atmospheric state or due to the limited accuracy of the MT_CKD water vapour scheme used in JURASSIC (Sect. 3.1), or if it is a real phenomenon depending on atmospheric water vapour concentrations. However, since the clear air simulations with low ACI values fall well below the aerosol detection threshold, this issue has no further implications for MIPAS aerosol detections.

4 Examples for application and verification

We applied our new aerosol detection method to the MIPAS measurements in 2011. We detected aerosol mainly after volcanic eruptions. In Fig. 6 three examples for aerosol detections after the Grímsvötn, Puyehue-Cordón Caulle, and Nabro eruption are presented. To verify our results we compared the MIPAS measurements with the AIRS SO_2 index and the AIRS ash index (both Hoffmann et al., 2014). High SO_2 index values indicate high SO_2 concentrations and high ash index values indicate high ash concentrations.

An U-shaped highly confined SO_2 filament was measured by AIRS on 27 May 2011, six days after the initial eruption of the Grímsvötn volcano (Fig. 6a). The black dashed curves indicate the MIPAS tracks measured between 00:00 and 12:00 UTC. Symbols along the MIPAS track indicate aerosol detections. The symbols are coloured in shades of blue and green representing the aerosol observation top altitude. In addition to our new aerosol detection method, we looked for volcanic ash using the volcanic ash detection method reported by Griessbach et al. (2014). As we could not detect volcanic ash in all four profiles, the aerosol particles are most likely sulfate aerosol. The SO_2 measured by AIRS is the precursor gas to sulfate aerosol measured by MIPAS. Since both species can be detected, the SO_2 oxidised only partially during the six days after the eruption and both measurements agree perfectly. While the AIRS data provide a high horizontal resolution picture of the volcanic plume the MIPAS data add altitude information.

AMTD
8, 4379–4412, 2015

In Fig. 6b the Nabro SO_2 plume is shown on 17 June 2014, three days after the initial eruption. The MIPAS tracks were measured between 00:00 and 12:00 UTC. The Nabro emissions were entrained in the Asian monsoon circulation and first were transported northwards and later on eastwards. Where MIPAS tracks cross the SO_2 plume measured by AIRS, MIPAS detects aerosol. The MIPAS ash index detected ash in 2 out of 20 aerosol profiles at altitudes below 10 km (over the Arabian peninsula and the Iranian plateau). From this finding we conclude that the Nabro plume mainly consists of sulfate aerosol, especially at higher altitudes. There are also some aerosol detections over the North Sea and northern Russia at altitudes below 12 km that do not coincide with enhanced SO_2. Tracing these aerosol detections back with the MIPAS measurements we found that these aerosol particles originated from the Grímsvötn eruption about one month earlier. The SO_2 from this eruption completely oxidised to sulfate aerosol and hence, is no longer seen in the AIRS SO_2 measurements anymore.

The AIRS SO_2 index in Fig. 6c and the ash index in Fig. 6d were measured on 9 June 2011, three days after the initial eruption of the Puyehue-Cordón Caulle. The corresponding MIPAS tracks were measured between 12:00 and 24:00 UTC. Aerosol detections above 18 km are coloured in black and are related to non-ice PSCs that are present in each Antarctic winter. Due to a strong jet stream the volcanic emissions were transported eastwards very quickly. The SO_2 plume in Fig. 6c stretches from the southern tip of Africa to the Indian Ocean just south west of Australia. Very close to this plume front there are six MIPAS profiles in a row indicating aerosol. These MIPAS detections are slightly westward of the plume front measured by AIRS, which is due to a temporal shift (up to 12 h) between the AIRS and MIPAS measurements. Along the filament extending south of Africa there are further matching MIPAS aerosol detections. However, MIPAS also detects aerosol over South Africa and along the way back to South America, where no enhanced SO_2 is visible in the AIRS data. Again, we looked for volcanic ash in the MIPAS data and found ash in 10 out of 16 aerosol profiles. That the Puyehue-Cordón Caulle plume was rich in ash, is also confirmed by the AIRS ash

AMTD
8, 4379–4412, 2015

index shown in Fig. 6d. The comparison of the MIPAS aerosol detections with the AIRS ash detections shows a good agreement.

For the three examples of fresh volcanic plumes in the polar, mid-latitude, and tropical atmosphere we found that the aerosol detection method introduced for infrared limb emission measurements performs well and also agrees well with AIRS volcanic emission measurements. However, in contrast to AIRS volcanic emission measurements the MIPAS measurements can trace volcanic ash and sulfur for much longer time scales (e.g. from June 2011 until 2012 in case of the Nabro eruption). The examples also demonstrate that infrared limb emission measurements provide valuable altitude information. In a recent visualisation study Günther et al. (2015) reconstructed 3-D volcanic emission plumes of the Nabro and Puyehue-Cordón Caulle by combining MIPAS aerosol and AIRS volcanic emission measurements with forward and backward trajectories started at the location of MIPAS aerosol detections.

5 Summary and conclusions

We introduced a two step method to detect aerosol in the troposphere and stratosphere with infrared limb emission measurements. In the first step we identified a window region in the MIPAS spectra that is sensitive toward aerosol and clouds. In addition to the widely used cloud index CI that is very sensitive to clouds we defined the aerosol index AI that is more sensitive to aerosol by using the identified window at 960 cm^{-1}. The AI has the advantage of being less altitude dependent in the troposphere in contrast to the CI. We combined the advantages of the AI in the troposphere and the CI in the stratosphere in a new index, the ACI, which is the maximum of the CI and the AI. The ACI is more sensitive towards aerosol and provides a better contrast to clear air over the whole UTLS than the CI. Instead of varying threshold values ranging from 2 to 6 depending on altitude, region and season for the CI, we found that an ACI < 7 is an appropriate global threshold value for the detection of enhanced aerosol and clouds.

AMTD
8, 4379–4412, 2015

In the second step we developed a method to discriminate between ice clouds and aerosol for infrared limb emission spectra with an ACI below 7. We used measured MIPAS spectra and simulations of optical properties for ice and volcanic aerosol employing typical size distributions (volcanic ash and sulfate aerosol) to identify appropriate windows for the discrimination. Three windows at 830, 960, and 1224 cm^{-1} that sample the contrasting behaviour of ice and aerosol are combined by brightness temperature difference correlations. We investigated the BTD correlations for the MIPAS measurements and selected scenarios where we expected to find ice clouds only, significant amounts of volcanic ash, volcanic sulfate aerosol, or non-ice PSCs. From these measurements we derived two threshold functions that discriminate between ice clouds and aerosol.

To corroborate and further characterise the threshold functions we analysed radiative transfer simulations of 1 km thick ice clouds and aerosol layers. The simulations confirmed that ice clouds fall below the thresholds and aerosol can exceed the thresholds. Only for the rare case of optically thick ($\beta_e = 5 \times 10^{-2}$ km^{-1} and larger) ice clouds at 18 km altitude in the tropics could the threshold function be exceeded (7 out of 3333 scenarios). However, we consider these scenarios to be very unlikely and found this confirmed by the measurements. In 2003(2011) only 0.02 %(0.08 %) of all tropical profiles (18 out of 74 767 and 62 out of 78 563) with an ACI smaller than 7 exceeded the threshold function in the potentially ambiguous BTD range (larger than −25 K for the BTD between the 830 and 1224 cm^{-1} windows). The simulations further showed that all realistic sulfate aerosol scenarios with $\beta_e(948\,cm^{-1}) > 1 \times 10^{-4}$ km^{-1} above 8 km tangent altitude can be discriminated from ice clouds. For ash clouds the simulations showed that several scenarios can be distinguished from ice clouds. Detectable ash cloud scenarios had extinction coefficients (at 948 cm^{-1}) between 1×10^{-4} and 5×10^{-1} km^{-1}, median radii between 0.3 and 5 µm and reached down to 6 km tangent altitude.

A comparison of MIPAS measurements with horizontally high resolution AIRS SO_2 and ash index measurements for three strong volcanic eruptions in 2011 that

AMTD
8, 4379–4412, 2015

were either characterised by large SO_2 (Grímsvötn, Nabro) or volcanic ash amounts (Puyehue-Cordón Caulle) demonstrated the viability of our aerosol detection method. This comparison and a very recent study (Günther et al., 2015) also point to the additional benefit of MIPAS altitude resolved volcanic aerosol detection. The infrared limb measurements can be used to quickly assign an altitude to the volcanic plume filaments measured by nadir instruments with high horizonal resolution.

We consider our new aerosol detection method to be adaptable to other hyperspectral infrared limb instruments such as CRISTA, CRISTA-NF, MIPAS balloon (MIPAS-B) (Oelhaf et al., 1994), MIPAS-STRatospheric aircraft (MIPAS-STR) (Woiwode et al., 2012), and Gimballed Limb Observer for Radiance Imaging of the Atmosphere (GLORIA) (Friedl-Vallon et al., 2014; Riese et al., 2014). Although MIPAS is no longer operating there are 10 years of MIPAS measurements available and the new aerosol detection method in conjunction with the volcanic ash detection method (Griessbach et al., 2014) opens up new perspectives for the analysis of enhanced aerosol in the UTLS and volcanic eruptions based on infrared limb emission measurements.

Acknowledgements. The MIPAS data were provided by the European Space Agency. The AIRS data were obtained from the NASA Goddard Earth Sciences Data Information and Services Center (GES DISC). The simulations were performed on JUROPA at Forschungszentrum Jülich. We gratefully acknowledge the computing time granted on the supercomputer at Jülich Supercomputing Centre (JSC). We are grateful to Thomas Kirchartz for discussions and comments on the manuscript. We also thank W. Lahoz for a grammatical and stylistic revision of the manuscript.

The article processing charges for this open-access publication were covered by a Research Centre of the Helmholtz Association.

AMTD
8, 4379–4412, 2015

References

Aumann, H., Chahine, M., Gautier, C., Goldberg, M., Kalnay, E., McMillin, L., Revercomb, H., Rosenkranz, P., Smith, W., Staelin, D., Strow, L., and Susskind, J.: AIRS/AMSU/HSB on the Aqua mission: design, science objectives, data products, and processing systems, IEEE T. Geosci. Remote, 41, 253–264, doi:10.1109/TGRS.2002.808356, 2003. 4383

Bauman, J. J., Russell, P. B., Geller, M. A., and Hamill, P.: A stratospheric aerosol climatology from SAGE II and CLAES measurements: 2. Results and comparisons, 1984–1999, J. Geophys. Res., 108, 4383, doi:10.1029/2002JD002993, 2003. 4381

Bourassa, A. E., Robock, A., Randel, W. J., Deshler, T., Rieger, L. A., Lloyd, N. D., Llewellyn, E. J. T., and Degenstein, D. A.: Large volcanic aerosol load in the stratosphere linked to Asian Monsoon transport, Science, 337, 78–81, doi:10.1126/science.1219371, 2012. 4386

Casadevall, T.: The 1989–1990 eruption of Redoubt volcano, Alaska – impacts on aircraft operations, J. Volcanol. Geoth. Res., 62, 301–316, doi:10.1016/0377-0273(94)90038-8, 1994. 4380

Clarisse, L., Hurtmans, D., Prata, A. J., Karagulian, F., Clerbaux, C., De Maziere, M., and Coheur, P.-F.: Retrieving radius, concentration, optical depth, and mass of different types of aerosols from high-resolution infrared nadir spectra, Appl. Optics, 49, 3713–3722, 2010. 4381

Clarisse, L., Coheur, P.-F., Prata, F., Hadji-Lazaro, J., Hurtmans, D., and Clerbaux, C.: A unified approach to infrared aerosol remote sensing and type specification, Atmos. Chem. Phys., 13, 2195–2221, doi:10.5194/acp-13-2195-2013, 2013. 4381

Clough, S., Shephard, M. W., Mlawer, E. J., Delamere, J. S., Iacono, M. J., Cady-Pereira, K., Boukabara, S., and Brown, P. D.: Atmospheric radiative transfer modeling: a summary of the AER codes, J. Quant. Spectrosc. Ra., 91, 233–244, 2005. 4387

de Reus, M., Borrmann, S., Bansemer, A., Heymsfield, A. J., Weigel, R., Schiller, C., Mitev, V., Frey, W., Kunkel, D., Kürten, A., Curtius, J., Sitnikov, N. M., Ulanovsky, A., and Ravegnani, F.: Evidence for ice particles in the tropical stratosphere from in-situ measurements, Atmos. Chem. Phys., 9, 6775–6792, doi:10.5194/acp-9-6775-2009, 2009. 4391, 4392

Deshler, T., Peter, T., Müller, R., and Crutzen, P.: The lifetime of Leewave-induced ice particles in the Arctic stratosphere.1. Balloonborne observations, Geophys. Res. Lett., 21, 1327–1330, 1994. 4391

AMTD
8, 4379–4412, 2015

Echle, G., von Clarmann, T., and Oelhaf, H.: Optical and microphysical parameters of the Mt. Pinatubo aerosol as determined from MIPAS-B mid-IR limb emission spectra, J. Geophys. Res., 103, 19193–19211, 1998. 4381

ESA: ENVISAT MIPAS Localized calibrated emission spectra (ENVISAT.MIP.NL_1P), available at: https://earth.esa.int/web/guest/data-access/browse-data-products/-/article/mipas-localized-calibrated-emission-spectra-1541, last access: January, 2015. 4383

Fischer, H., Birk, M., Blom, C., Carli, B., Carlotti, M., von Clarmann, T., Delbouille, L., Dudhia, A., Ehhalt, D., Endemann, M., Flaud, J. M., Gessner, R., Kleinert, A., Koopman, R., Langen, J., López-Puertas, M., Mosner, P., Nett, H., Oelhaf, H., Perron, G., Remedios, J., Ridolfi, M., Stiller, G., and Zander, R.: MIPAS: an instrument for atmospheric and climate research, Atmos. Chem. Phys., 8, 2151–2188, doi:10.5194/acp-8-2151-2008, 2008. 4381, 4383

Frey, W., Borrmann, S., Kunkel, D., Weigel, R., de Reus, M., Schlager, H., Roiger, A., Voigt, C., Hoor, P., Curtius, J., Krämer, M., Schiller, C., Volk, C. M., Homan, C. D., Fierli, F., Di Donfrancesco, G., Ulanovsky, A., Ravegnani, F., Sitnikov, N. M., Viciani, S., D'Amato, F., Shur, G. N., Belyaev, G. V., Law, K. S., and Cairo, F.: In situ measurements of tropical cloud properties in the West African Monsoon: upper tropospheric ice clouds, Mesoscale Convective System outflow, and subvisual cirrus, Atmos. Chem. Phys., 11, 5569–5590, doi:10.5194/acp-11-5569-2011, 2011. 4391, 4392

Fridlind, A. M., Ackerman, A. S., Jensen, E. J., Heymsfield, A. J., Poellot, M. R., Stevens, D. E., Wang, D. H., Miloshevich, L. M., Baumgardner, D., Lawson, R. P., Wilson, J. C., Flagan, R. C., Seinfeld, J. H., Jonsson, H. H., VanReken, T. M., Varutbangkul, V., and Rissman, T. A.: Evidence for the predominance of mid-tropospheric aerosols as subtropical anvil cloud nuclei, Science, 304, 718–722, 2004. 4380

Friedl-Vallon, F., Gulde, T., Hase, F., Kleinert, A., Kulessa, T., Maucher, G., Neubert, T., Olschewski, F., Piesch, C., Preusse, P., Rongen, H., Sartorius, C., Schneider, H., Schönfeld, A., Tan, V., Bayer, N., Blank, J., Dapp, R., Ebersoldt, A., Fischer, H., Graf, F., Guggenmoser, T., Höpfner, M., Kaufmann, M., Kretschmer, E., Latzko, T., Nordmeyer, H., Oelhaf, H., Orphal, J., Riese, M., Schardt, G., Schillings, J., Sha, M. K., Suminska-Ebersoldt, O., and Ungermann, J.: Instrument concept of the imaging Fourier transform spectrometer GLORIA, Atmos. Meas. Tech., 7, 3565–3577, doi:10.5194/amt-7-3565-2014, 2014. 4398

AMTD
8, 4379–4412, 2015

Fromm, M., Kablick, III, G., Nedoluha, G., Carboni, E., Grainger, R., Campbell, J., and Lewis, J.: Correcting the record of volcanic stratospheric aerosol impact: Nabro and Sarychev Peak, J. Geophys. Res., 119, 10343–10364, doi:10.1002/2014JD021507, 2014. 4386

Gordley, L. L. and Russell, J. M.: Rapid inversion of limb radiance data using an emissivity growth approximation, Appl. Optics, 20, 807–813, 1981. 4384

Grainger, R. G., Lambert, A., Taylor, F. W., Remedios, J. J., Rodgers, C. D., Corney, M., and Kerridge, B. J.: Infrared-absorption by volcanic stratospheric aerosols observed by ISAMS, Geophys. Res. Lett., 20, 1283–1286, doi:10.1029/93GL00823, 1993. 4381

Grainger, R. G., Peters, D. M., Thomas, G. E., Smith, A. J. A., Siddans, R., Carboni, E., and Dudhia, A.: Measuring volcanic plume and ash properties from space, in: Remote-sensing of Volcanoes and Volcanic Processes: Integrating Observation and Modelling, edited by: Pyle, D., Mather, T., and Biggs, J., The Geological Society Special Publication, 380, 293–320, doi:10.1144/SP380.7, 2013. 4382

Grießbach, S.: Clouds and aerosol in infrared radiative transfer calculations for the analysis of satellite observations, vol. 139 of Schriften des Forschungszentrums Jülich, Reihe Energie & Umwelt, Forschungszentrum Jülich, Jülich, available at: http://juwel.fz-juelich.de:8080/dspace/handle/2128/4597 (last access: 24 July 2014), 2012. 4384

Griessbach, S., Hoffmann, L., von Hobe, M., Müller, R., Spang, R., and Riese, M.: A six-year record of volcanic ash detection with Envisat MIPAS, in: Proceedings of ESA ATMOS 2012, European Space Agency, Bruges, Belgium, 18–22 June 2012, ESA Special Publication SP-708 (CD-ROM), 2012. 4382

Griessbach, S., Hoffmann, L., Hoepfner, M., Riese, M., and Spang, R.: Scattering in infrared radiative transfer: a comparison between the spectrally averaging model JURASSIC and the line-by-line model KOPRA, J. Quant. Spectrosc. Ra., 27, 102–118, doi:10.1016/j.jqsrt.2013.05.004, 2013. 4384, 4387

Griessbach, S., Hoffmann, L., Spang, R., and Riese, M.: Volcanic ash detection with infrared limb sounding: MIPAS observations and radiative transfer simulations, Atmos. Meas. Tech., 7, 1487–1507, doi:10.5194/amt-7-1487-2014, 2014. 4382, 4384, 4388, 4389, 4391, 4393, 4394, 4398

Griessbach, S., Hoffmann, L., Spang, R., Riese, M., and more: Characterisation of the MIPAS Aerosol Top Altitude, Atmos. Meas. Tech. Discuss., in preparation, 2015. 4392

Grimsdell, A. W., Alexander, M. J., May, P. T., and Hoffmann, L.: Model study of waves generated by convection with direct validation via satellite, J. Atmos. Sci., 67, 1617–1631, 2010. 4384

AMTD
8, 4379–4412, 2015

Günther, T., Schulze, M., Friederici, A., and Theisel, H.: 2014 IEEE Scientific Visualization Contest Winner: visualizing volcanic clouds in the atmosphere and their impact on air traffic, IEEE Computer Graphics and Applications, accepted, in press, 2015. 4396, 4398

Hoffmann, L. and Alexander, M. J.: Retrieval of stratospheric temperatures from Atmospheric Infrared Sounder radiance measurements for gravity wave studies, J. Geophys. Res., 114, D07105, doi:10.1029/2008JD011241, 2009. 4384

Hoffmann, L., Kaufmann, M., Spang, R., Müller, R., Remedios, J. J., Moore, D. P., Volk, C. M., von Clarmann, T., and Riese, M.: Envisat MIPAS measurements of CFC-11: retrieval, validation, and climatology, Atmos. Chem. Phys., 8, 3671–3688, doi:10.5194/acp-8-3671-2008, 2008. 4384

Hoffmann, L., Weigel, K., Spang, R., Schroeder, S., Arndt, K., Lehmann, C., Kaufmann, M., Ern, M., Preusse, P., Stroh, F., and Riese, M.: CRISTA-NF measurements of water vapor during the SCOUT-O3 Tropical Aircraft Campaign, Adv. Space Res., 43, 74–81, 2009. 4384

Hoffmann, L., Griessbach, S., and Meyer, C. I.: Volcanic emissions from AIRS observations: detection methods, case study, and statistical analysis, in: Proceedings of SPIE Volume 9242, Remote Sensing of Clouds and the Atmosphere XIX; and Optics in Atmospheric Propagation and Adaptive Systems XVII, SPIE Remote Sensing Europe, Amsterdam, the Netherlands, 22 September 2014, 924214, doi:10.1117/12.2066326, 2014. 4394

Höpfner, M., Pitts, M. C., and Poole, L. R.: Comparison between CALIPSO and MIPAS observations of polar stratospheric clouds, J. Geophys. Res., 114, D00H05, doi:10.1029/2009JD012114, 2009. 4381

Hummel, J. R., Shettle, E. P., and Longtin, D. R.: A New Background Stratospheric Aerosol Model for Use in Atmospheric Radiation Models, AFGL-TR-88-0166, Air Force Geophysics Laboratory, Hanscom AFB, MA, 1988. 4388

Iwasaki, S., Maruyama, K., Hayashi, M., Ogino, S.-Y., Ishimoto, H., Tachibana, Y., Shimizu, A., Matsui, I., Sugimoto, N., Yamashita, K., Saga, K., Iwamoto, K., Kamiakito, Y., Chabangborn, A., Thana, B., Hashizume, M., Koike, T., and Oki, T.: Characteristics of aerosol and cloud particle size distributions in the tropical tropopause layer measured with optical particle counter and lidar, Atmos. Chem. Phys., 7, 3507–3518, doi:10.5194/acp-7-3507-2007, 2007. 4391

Karagulian, F., Clarisse, L., Clerbaux, C., Prata, A. J., Hurtmans, D., and Coheur, P. F.: Detection of volcanic SO_2, ash, and H_2SO_4 using the Infrared Atmospheric Sounding Interferometer (IASI), J. Geophys. Res., 115, D00L02, doi:10.1029/2009JD012786, 2010. 4381

AMTD
8, 4379–4412, 2015

Koren, I., Kaufman, Y. J., Washington, R., Todd, M. C., Rudich, Y., Martins, J. V., and Rosenfeld, D.: The Bodele depression: a single spot in the Sahara that provides most of the mineral dust to the Amazon forest, Environ. Res. Lett., 1, 014005, doi:10.1088/1748-9326/1/1/014005, 2006. 4380

Lambert, A., Grainger, R. G., Remedios, J. J., Rodgers, C. D., Corney, M., and Taylor, F. W.: Measurements of the evolution of the Mt. Pinatubo aerosol cloud by ISAMS, Geophys. Res. Lett., 20, 1287–1290, doi:10.1029/93GL00827, 1993. 4381

Lambert, A., Grainger, R. G., Rodgers, C. D., Taylor, F. W., Mergenthaler, J. L., Kumer, J. B., and Massie, S. T.: Global evolution of the Mt Pinatubo volcanic aerosols observed by the infrared limb-sounding instruments CLAES and ISAMS on the Upper Atmosphere Research Satellite, J. Geophys. Res., 102, 1495–1512, doi:10.1029/96JD00096, 1997. 4381

Massie, S. T., Deshler, T., Thomas, G. E., Mergenthaler, J. L., and Russell, J. M.: Evolution of the infrared properties of the Mount Pinatubo aerosol cloud over Laramie, Wyoming, J. Geophys. Res., 101, 23007–23019, 1996. 4381

Oelhaf, H., von Clarmann, T., Fischer, H., Friedl-Vallon, F., Fritzsche, C., Linden, A., Piesch, C., Seefeldner, M., and Volker, W.: Stratospheric $ClONO_2$ and HNO_3 profiles inside the Arctic vortex from MIPAS-B limb emission-spectra obtained during EASOE, Geophys. Res. Lett., 21, 1263–1266, doi:10.1029/93GL01303, 1994. 4398

Offermann, D., Grossmann, K.-U., Barthol, P., Knieling, P., Riese, M., and Trant, R.: Cryogenic Infrared Spectrometers and Telescopes for the Atmosphere (CRISTA) experiment and middle atmosphere variability, J. Geophys. Res., 104, 16311–16325, 1999. 4381

Pollack, J., Toon, O., and Khare, B.: Optical properties of some terrestrial rocks and glasses, Icarus, 19, 372–389, doi:10.1016/0019-1035(73)90115-2, 1973. 4388, 4393, 4411

Remedios, J. J., Leigh, R. J., Waterfall, A. M., Moore, D. P., Sembhi, H., Parkes, I., Greenhough, J., Chipperfield, M.P., and Hauglustaine, D.: MIPAS reference atmospheres and comparisons to V4.61/V4.62 MIPAS level 2 geophysical data sets, Atmos. Chem. Phys. Discuss., 7, 9973–10017, doi:10.5194/acpd-7-9973-2007, 2007. 4387

Ridley, D. A., Solomon, S., Barnes, J. E., Burlakov, V. D., Deshler, T., Dolgii, S. I., Herber, A. B., Nagai, T., Neely, III, R. R., Nevzorov, A. V., Ritter, C., Sakai, T., Santer, B. D., Sato, M., Schmidt, A., Uchino, O., and Vernier, J. P.: Total volcanic stratospheric aerosol optical depths and implications for global climate change, Geophys. Res. Lett., 41, 7763–7769, doi:10.1002/2014GL061541, 2014. 4380, 4381, 4382

AMTD
8, 4379–4412, 2015

Riese, M., Spang, R., Preusse, P., Ern, M., Jarisch, M., Offermann, D., and Grossmann, K. U.: Cryogenic Infrared Spectrometers and Telescopes for the Atmosphere (CRISTA) data processing and atmospheric temperature and trace gas retrieval, J. Geophys. Res., 104, 16349–16367, 1999. 4381

Riese, M., Oelhaf, H., Preusse, P., Blank, J., Ern, M., Friedl-Vallon, F., Fischer, H., Guggenmoser, T., Höpfner, M., Hoor, P., Kaufmann, M., Orphal, J., Plöger, F., Spang, R., Suminska-Ebersoldt, O., Ungermann, J., Vogel, B., and Woiwode, W.: Gimballed Limb Observer for Radiance Imaging of the Atmosphere (GLORIA) scientific objectives, Atmos. Meas. Tech., 7, 1915–1928, doi:10.5194/amt-7-1915-2014, 2014. 4398

Santer, B. D., Bonfils, C., Painter, J. F., Zelinka, M. D., Mears, C., Solomon, S., Schmidt, G. A., Fyfe, J. C., Cole, J. N. S., Nazarenko, L., Taylor, K. E., and Wentz, F. J.: Volcanic contribution to decadal changes in tropospheric temperature, Nat. Geosci., 7, 185–189, doi:10.1038/NGEO2098, 2014. 4380

Sembhi, H., Remedios, J., Trent, T., Moore, D. P., Spang, R., Massie, S., and Vernier, J.-P.: MIPAS detection of cloud and aerosol particle occurrence in the UTLS with comparison to HIRDLS and CALIOP, Atmos. Meas. Tech., 5, 2537–2553, doi:10.5194/amt-5-2537-2012, 2012. 4382, 4385

Spang, R. and Remedios, J. J.: Observations of a distinctive infra-red spectral feature in the atmospheric spectra of polar stratospheric clouds measured by the CRISTA instrument, Geophys. Res. Lett., 30, 1875, doi:10.1029/2003GL017231, 2003. 4381

Spang, R., Riese, M., and Offermann, D.: CRISTA-2 observations of the south polar vortex in winter 1997: a new dataset for polar process studies, Geophys. Res. Lett., 28, 3159–3162, doi:10.1029/2000GL012374, 2001. 4382, 4385

Spang, R., Remedios, J. J., and Barkley, M. P.: Colour indices for the detection and differentiation of cloud type in infra-red limb emission spectra, Adv. Space Res., 33, 1041–1047, 2004. 4381, 4382, 4385, 4386

Spang, R., Remedios, J. J., Tilmes, S., and Riese, M.: MIPAS observation of polar stratospheric clouds in the Arctic 2002/2003 and Antarctic 2003 winters, Adv. Space Res., 36, 868–878, doi:10.1016/j.asr.2005.03.092, 2005. 4381

Spang, R., Hoffmann, L., Kullmann, A., Olschewski, F., Preusse, P., Knieling, P., Schroeder, S., Stroh, F., Weigel, K., and Riese, M.: High resolution limb observations of clouds by the CRISTA-NF experiment during the SCOUT-O3 tropical aircraft campaign, Adv. Space Res., 42, 1765–1775, doi:10.1016/j.asr.2007.09.036, 2008. 4382

AMTD
8, 4379–4412, 2015

Spang, R., Arndt, K., Dudhia, A., Höpfner, M., Hoffmann, L., Hurley, J., Grainger, R. G., Griessbach, S., Poulsen, C., Remedios, J. J., Riese, M., Sembhi, H., Siddans, R., Waterfall, A., and Zehner, C.: Fast cloud parameter retrievals of MIPAS/Envisat, Atmos. Chem. Phys., 12, 7135–7164, doi:10.5194/acp-12-7135-2012, 2012. 4381, 4382, 4385

Ungermann, J., Kaufmann, M., Hoffmann, L., Preusse, P., Oelhaf, H., Friedl-Vallon, F., and Riese, M.: Towards a 3-D tomographic retrieval for the air-borne limb-imager GLORIA, Atmos. Meas. Tech., 3, 1647–1665, doi:10.5194/amt-3-1647-2010, 2010. 4384

Vernier, J. P., Thomason, L. W., Pommereau, J. P., Bourassa, A., Pelon, J., Garnier, A., Hauchecorne, A., Blanot, L., Trepte, C., Degenstein, D., and Vargas, F.: Major influence of tropical volcanic eruptions on the stratospheric aerosol layer during the last decade, Geophys. Res. Lett., 38, L12807, doi:10.1029/2011GL047563, 2011. 4380, 4381

Volz, F. E.: Infrared optical constants of ammonium sulfate, Sahara dust, volcanic pumice and fly ash, Appl. Optics, 12, 564–568, 1973. 4388, 4393

Warren, S. G. and Brandt, R. E.: Optical constants of ice from the ultraviolet to the microwave: a revised compilation, J. Geophys. Res., 113, D14220, doi:10.1029/2007JD009744, 2008. 4388

Weigel, K., Riese, M., Hoffmann, L., Hoefer, S., Kalicinsky, C., Knieling, P., Olschewski, F., Preusse, P., Spang, R., Stroh, F., and Volk, C. M.: CRISTA-NF measurements during the AMMA-SCOUT-O3 aircraft campaign, Atmos. Meas. Tech., 3, 1437–1455, doi:10.5194/amt-3-1437-2010, 2010. 4384

Woiwode, W., Oelhaf, H., Gulde, T., Piesch, C., Maucher, G., Ebersoldt, A., Keim, C., Höpfner, M., Khaykin, S., Ravegnani, F., Ulanovsky, A. E., Volk, C. M., Hösen, E., Dörnbrack, A., Ungermann, J., Kalicinsky, C., and Orphal, J.: MIPAS-STR measurements in the Arctic UTLS in winter/spring 2010: instrument characterization, retrieval and validation, Atmos. Meas. Tech., 5, 1205–1228, doi:10.5194/amt-5-1205-2012, 2012. 4398

Yu, F. Q., Luo, G., Bates, T. S., Anderson, B., Clarke, A., Kapustin, V., Yantosca, R. M., Wang, Y. X., and Wu, S. L.: Spatial distributions of particle number concentrations in the global troposphere: simulations, observations, and implications for nucleation mechanisms, J. Geophys. Res., 115, D17205, doi:10.1029/2009JD013473, 2010. 4380

Yuan, T., Remer, L. A., and Yu, H.: Microphysical, macrophysical and radiative signatures of volcanic aerosols in trade wind cumulus observed by the A-Train, Atmos. Chem. Phys., 11, 7119–7132, doi:10.5194/acp-11-7119-2011, 2011. 4380

AMTD
8, 4379–4412, 2015

Zhang, X., Rao, R., Huang, Y., Mao, M., Berg, M. J., and Sun, W.: Black carbon aerosols in urban central China, J. Quant. Spectrosc. Ra., 150, 3–11, doi:10.1016/j.jqsrt.2014.03.006, 2015. 4380

AMTD
8, 4379–4412, 2015

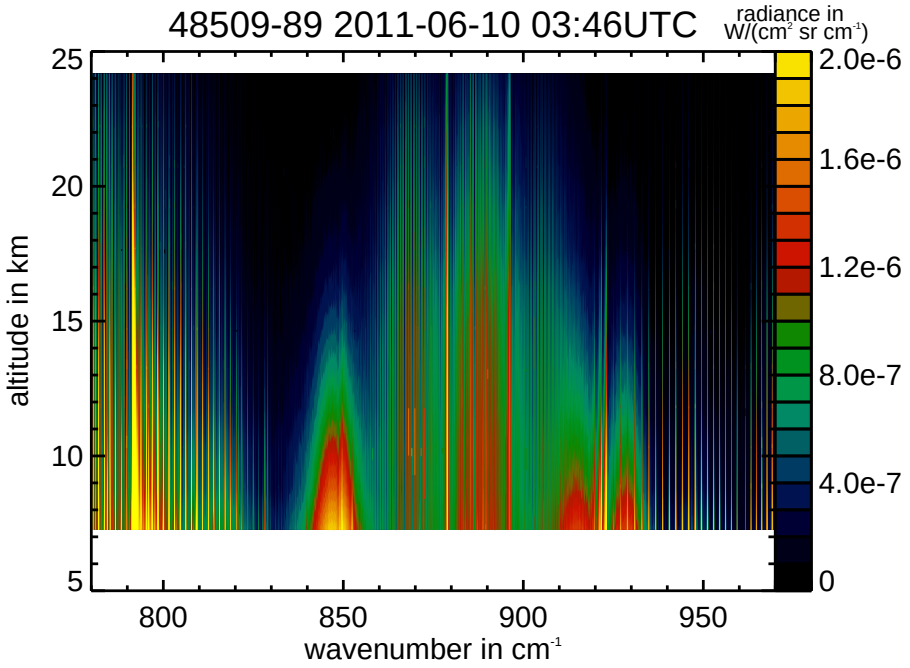

Figure 1. MIPAS radiances measured in profile 89 of orbit 48 509 (around 48° S). This clear air case shows low radiances in the broad window region around 830 cm^{-1} and multiple narrow windows between 950–970 cm^{-1}.

AMTD
8, 4379–4412, 2015

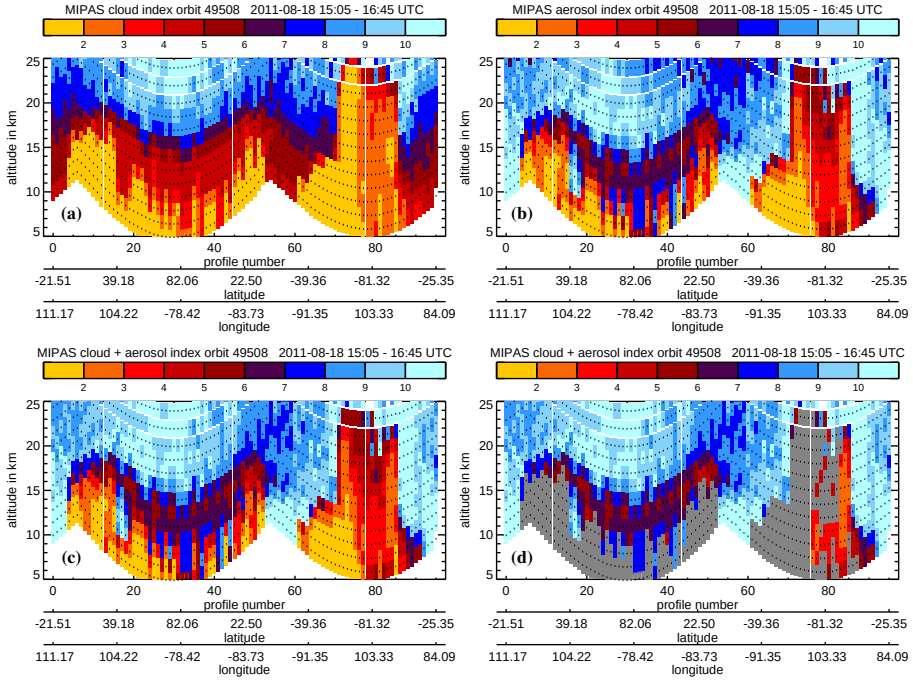

Figure 2. MIPAS profiles of orbit 49 508 measured on 18 August 2011. Shown are **(a)** cloud index, **(b)** aerosol index, **(c)** aerosol-cloud index, **(d)** aerosol-cloud index for clear air and aerosol. Ice and optically thick clouds (grey body radiators) are shown in grey.

AMTD
8, 4379–4412, 2015

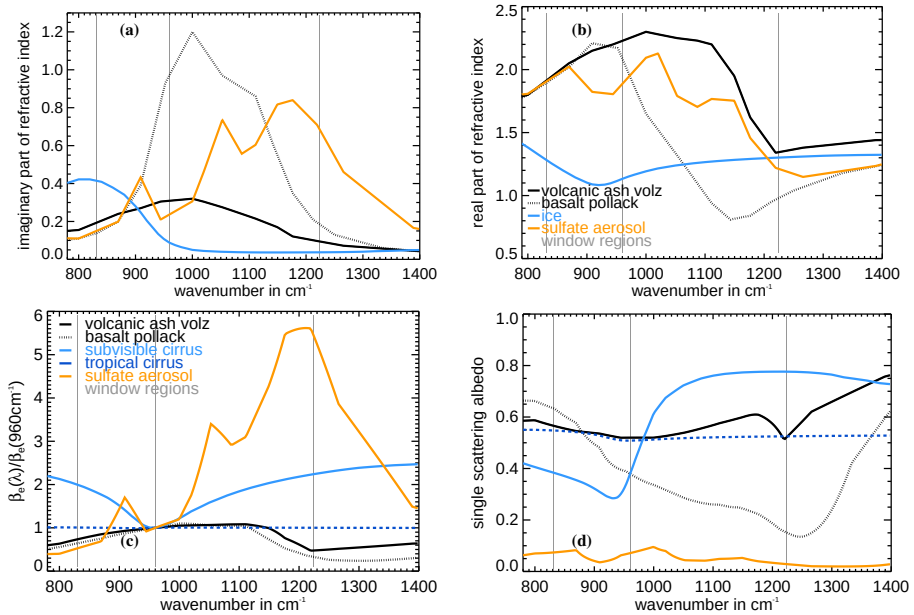

Figure 3. Microphysical properties of sulfate aerosol, ice, and two types of volcanic ash: **(a, b)** complex refractive indices and their optical properties: **(c)** extinction coefficient and **(d)** single scattering albedo. The vertical lines indicate atmospheric window regions.

AMTD
8, 4379–4412, 2015

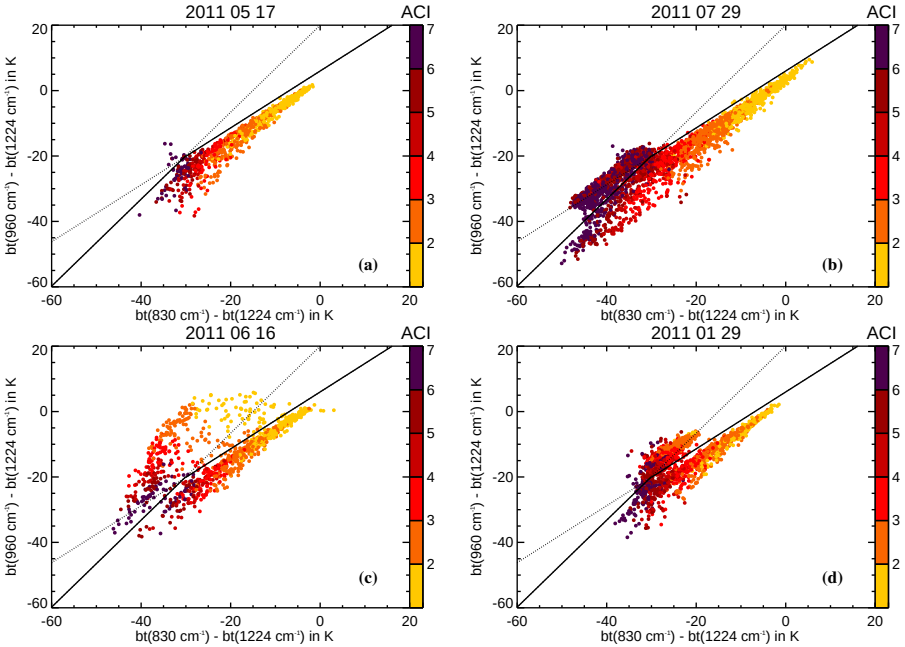

Figure 4. MIPAS brightness temperature difference correlations for selected scenarios: **(a)** ice clouds (0–60° S), **(b)** Nabro sulfate aerosol (0–90° N) and ice clouds, **(c)** Puyehue-Cordón Caulle volcanic ash (0–60° S) and ice clouds, and **(d)** PSCs (0–90° N) and ice clouds. All figures comprise measurements of a single day, which are about 14 orbits. The black lines are the classification thresholds derived from the observations, where the solid part of each line denotes the relevant part for the discrimination between aerosol and ice.

AMTD
8, 4379–4412, 2015

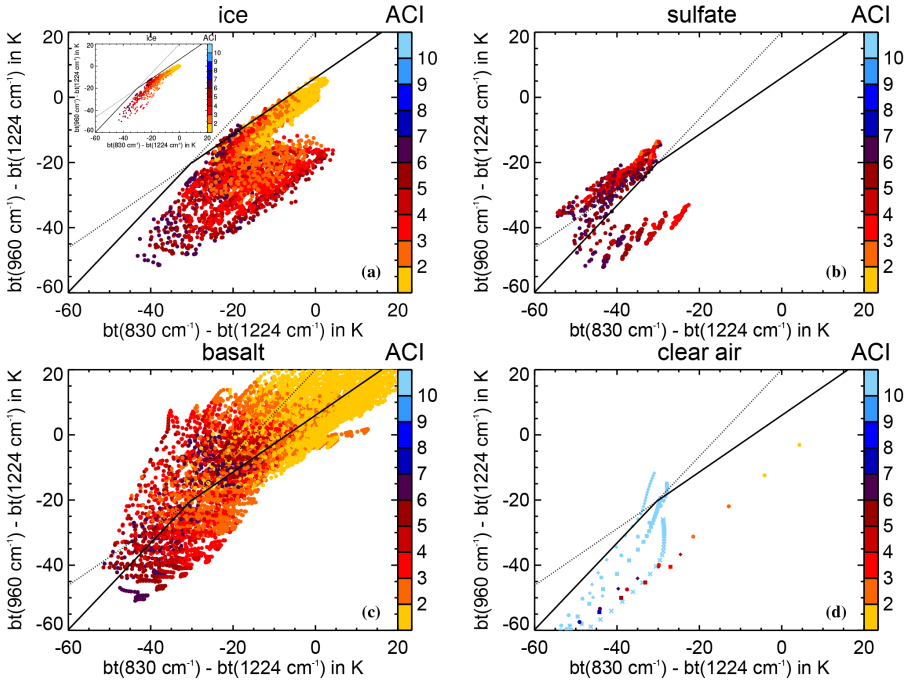

Figure 5. Simulated brightness temperature difference correlations for: **(a)** ice clouds, **(b)** sulfate aerosol, **(c)** volcanic ash (here basalt from Pollack et al., 1973, is shown), and **(d)** clear air. The ice cloud simulations are shown for median radii ranging from 0.3 to 96 µm. In the small inset ice simulations are only shown for median radii ranging from 12 to 96 µm. For the clear air simulations the atmosphere type is indicated by the following symbols: polar winter – crosses, polar summer – diamonds, mid-latitudes – squares, equatorial – circles. The black lines are the classification thresholds derived from the observations, where the solid part of each line denotes the relevant part for the discrimination between aerosol and ice.

AMTD
8, 4379–4412, 2015

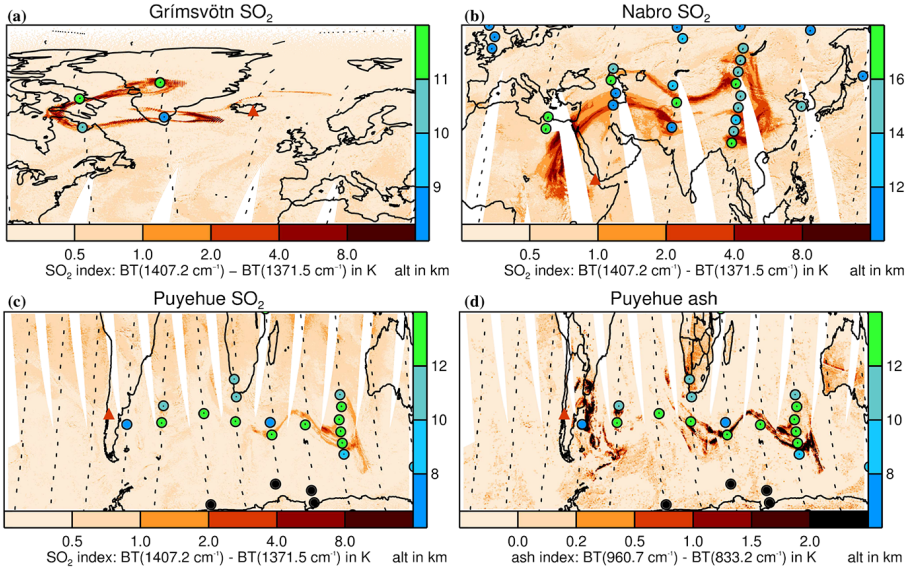

Figure 6. AIRS volcanic emission contours and MIPAS aerosol detections (coloured circles). **(a)** AIRS SO_2 index for Grímsvötn (27 May 2011 a.m.), **(b)** AIRS SO_2 index for Nabro (17 June 2011 a.m.), **(c)** AIRS SO_2 index for Puyehue-Cordón Caulle (9 June 2011 p.m.), **(d)** AIRS ash index for Puyehue-Cordón Caulle (9 June 2011 p.m.). Non-ice PSCs in the Antarctic at altitudes above 18 km are coloured in black. The red triangles indicate the location of the respective volcanoes. Please note the different altitude scales.

AMTD
8, 4379–4412, 2015